Optical phase estimation for a patch-type extrinsic Fabry–Perot interferometer sensor system and its application to flutter suppression

2005 Smart Mater. Struct. 14 696

(http://iopscience.iop.org/0964-1726/14/4/028)

INSTITUTE OF PHYSICS PUBLISHING SMART MATERIALS AND STRUCTURES
Smart Mater. Struct. **14** (2005) 696–706 doi:10.1088/0964-1726/14/4/028

Optical phase estimation for a patch-type extrinsic Fabry–Perot interferometer sensor system and its application to flutter suppression

Do-Hyung Kim[1], Young-Hwan Chang[2], Jae-Hung Han[2,3] and In Lee[2]

[1] Rotorcraft Department, Korea Aerospace Research Institute, 45 Eoeun-dong, Yuseoung-gu, Daejeon 305-333, Korea
[2] Department of Aerospace Engineering, Korea Advanced Institute of Science and Technology, 373-1 Guseong-dong, Yuseong-gu, Daejeon 305-701, Korea

E-mail: jaehunghan@kaist.ac.kr

Received 16 March 2004, in final form 14 December 2004
Published 29 June 2005
Online at stacks.iop.org/SMS/14/696

Abstract
An optical phase tracking technique for an extrinsic Fabry–Perot interferometer (EFPI) is proposed in order to overcome interferometric non-linearity. The basic idea is utilizing strain rate information, which cannot be easily obtained from the EFPI sensor itself. The proposed phase tracking system consists of a patch-type EFPI sensor and a simple on-line phase tracking logic. The patch-type EFPI sensor comprises an EFPI and a piezoelectric patch. An EFPI sensor itself has non-linear behavior due to the interferometric characteristics, and a piezoelectric material has hysteresis. However, the composed patch-type EFPI sensor system overcomes the problems that can arise when they are used individually. The proposed system can extract vibration information from severely distorted EFPI sensor signals. The dynamic characteristics of the proposed phase tracking system were investigated, and then the patch-type EFPI sensor system was applied to the active suppression of flutter, dynamic aeroelastic instability, of a swept-back composite plate structure. The real time neural predictive control algorithm effectively reduces the amplitude of the flutter mode, and 6.5% flutter speed enhancement for the aeroelastic system was obtained by integrating smart materials into advanced structures.

(Some figures in this article are in colour only in the electronic version)

1. Introduction

This paper proposes a simple phase tracking system for the extrinsic Fabry–Perot interferometer (EFPI) sensor for overcoming the interferometric non-linearity of the EFPI and experimentally demonstrates the performance of the proposed algorithms. The proposed phase tracking system consists of a patch-type EFPI sensor and an on-line phase tracking logic. The patch-type EFPI sensor comprises an EFPI and a piezoceramic (lead–zirconate–titanate, PZT) patch. An EFPI sensor itself has non-linear behavior due to the interferometric characteristics, and PZT has hysteresis. However, the composed patch-type EFPI sensor system overcomes the problems that may arise when they are used individually. Moreover, the proposed system can extract vibration information from the EFPI sensor signal with high non-linearity. In the first place, the dynamic characteristics of the proposed phase tracking system were investigated, and

[3] Author to whom any correspondence should be addressed.

then the proposed sensor system was applied to a practical situation: aeroelastic control of a plate structure.

Optical fiber sensor systems have been successfully applied in various engineering fields. Distributed sensing and monitoring of structures using optical fiber sensor networks is receiving increasing intention in the field of aircraft and spacecraft engineering, where the reliability of lightweight structure is the key particular. Among several kinds of optical fiber sensors, interferometric sensors are particularly widely used because they have many advantages of general optical sensors and can be constructed at reasonable prices. However, it is reported that they have a problem in representing vibrational amplitudes and directions accurately because of their interferometric characteristics. In order to extract true mechanical strain from the EFPI output signal, several methods have been proposed including quadrature phase-shifted EFPI [1], absolute EFPI (AEFPI) [2], and passive quadratic signal processing using two read-out interferometers [3]. Several signal processing techniques have also been used based on a fringe counting method [4, 5]. Such algorithms can be applicable to the measurement of strain of quasi-static systems, but are not practical for real time feedback control systems. Therefore, studies on vibration control using interferometric optical fiber sensors have been limited to small disturbance cases [6]. In the authors' previous work [7], we experimentally investigated vibration control performance when the EFPI sensor produces non-linear signals. We examined the effects of non-linearity of the sensor on the control stability and performance, and investigated a simple method applicable to the vibrations beyond the linear range. For this purpose, a neural controller was utilized and its performance was experimentally investigated. It was found that the neural network controller could suppress the non-linear vibration to some extent. However, an adaptive control algorithm such as a neural network is not a fundamental solution to a dynamic system with highly non-linear sensing characteristics. Therefore, this paper establishes a more practical method for extracting vibration information from the EFPI sensor signal.

For lightweight and flexible flight structures, it is important to measure and suppress flow-induced vibrations such as flutter caused by interactions between the fluid and structures. In recent years, several active control strategies have been studied in order to favorably modify the behavior of aeroelastic systems [8]. Active flutter suppression techniques can delay the onset of the flutter and enhance maneuverability. The Active Flexible Wing program has demonstrated flutter suppression of a fighter-type scaled model in various maneuvering modes, utilizing control surfaces and active control technology, at NASA Langley research center [9]. The benchmark active control technology (BACT) model has been used as an active control test bed for evaluating new and innovative control methodologies [10].

Recent development of smart materials and structures gives us another alternative for active flutter suppression. Lazarus *et al* [11] successfully applied multi-input multi-output controls to suppress vibration and flutter of a plate-like lifting surface with surface bonded piezoelectric actuators. Han *et al* [12] performed a numerical and experimental investigation on active flutter suppression of a swept-back cantilevered plate using modern robust control theory. Application of piezoelectric actuation to flutter control of a more realistic wing model was achieved under the Piezoelectric Aeroelastic Response Tailoring Investigation program at NASA Langley research center [13].

Since the aeroelastic phenomena are the result of the interactions between fluid and structures, dynamic characteristics of an aeroelastic system change according to the airflow speed. Therefore, it is difficult to obtain an exact numerical model, and the adaptiveness and robustness are important features for an aeroelastic control system. Control systems can be subdivided into two categories: highly specialized controllers and general purpose controllers. Highly specialized controllers are relevant when the system to be controlled is in some sense difficult to stabilize or when the performance is extremely important. General purpose controllers are such that the same controller structure can be used for a wide class of practical systems, and the controllers are characterized by being simple to tune so that a satisfactory performance can be achieved with a modest effort [14]. Basically, neural networks belong to the latter group, and their ability to model a wide class of systems in many applications can reduce time spent on development and offer a better performance than can be obtained with conventional techniques. At the same time, neural networks can be regarded as highly specialized controllers because of their successful applications to many non-linear and very specific systems. Among the many kinds of neural network based control systems, a neural predictive control (NPC) system was selected for consideration in the present study. The NPC is based on the generalized predictive control (GPC) framework with a neural network representing the plant dynamics. The GPC system is known to control non-minimum phase plants, open-loop unstable plants and plants with variable or unknown dead time. It is also reported to be robust with respect to modeling errors, overparameterization and underparameterization and sensor noise. For non-linear plants, the ability of GPC to make accurate predictions can be enhanced if a neural network is used to learn the dynamics of the plant instead of standard non-linear modeling techniques [15]. The NPC has been applied in various engineering fields. Gu and Hu [16] presented a path tracking scheme for a car-like mobile robot based on NPC. A multi-layer back-propagation neural network was employed to model the non-linear kinematics of the robot in order to adapt the robot to a large operating range. Tsai *et al* [17] applied a neural network model for a non-linear chemical process, a neutralization process. Of course, the application to vibration control is one of the most active research areas. In this study, a NPC system is designed and the control performance is investigated through ground and wind tunnel experiments.

In the authors' previous work [18], prediction and suppression of flutter using a fiber Bragg grating (FBG) sensor system were performed. In the study, a neural network control system with a neuroidentification model and neurocontroller was applied. While such a control system has good convergence characteristics, its convergence speed is not so fast that it is applicable to vibration suppression of structural systems with a control bandwidth of several tens of hertz. Therefore, a NPC system with fast calculation capability is constructed and used in the present study.

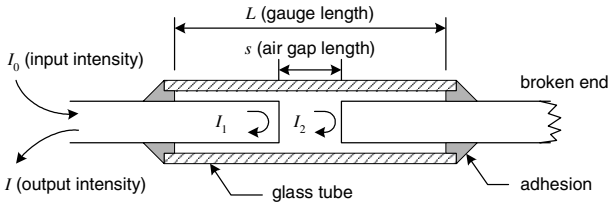

Figure 1. Schematic diagram of the EFPI.

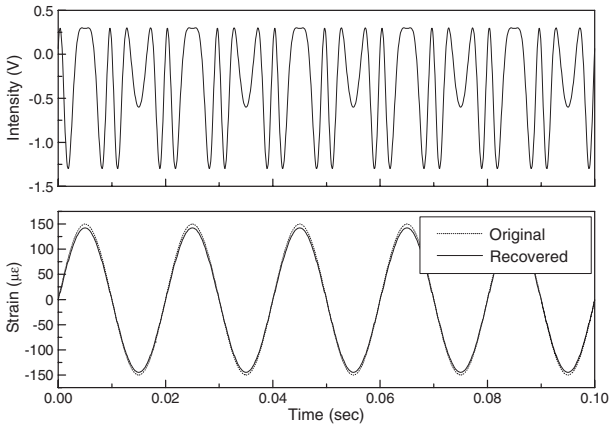

Figure 2. Simulation results for exact A and B.

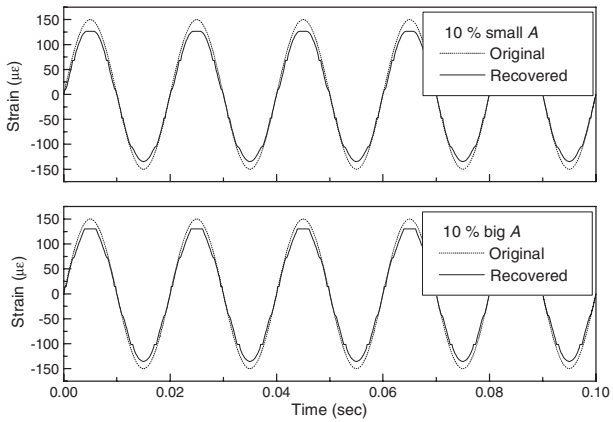

Figure 3. Simulation result with 10% error in A.

Table 1. Simulation parameters of an example system for phase tracking.

Parameters	Values
L	5 mm
A	−0.5
B	0.8
ϕ_0	$7\pi/4$ rad
Strain amplitude	150 $\mu\varepsilon$
Vibration frequency	50 Hz
Sampling frequency	5 kHz

2. On-line phase tracking method using strain rate information

The operating mechanism of an EFPI sensor can be found in [7]. Its schematic diagram is shown in figure 1, where the reflected optical intensity, I, can be written as a sinusoidal function as follows:

$$I = A + B\cos\phi \tag{1}$$

where A and B are functions of the fiber core radius, the air gap separation, the transmission coefficient of the air/glass interface and the numerical aperture; and ϕ is the optical phase. If the parameters A and B are assumed to be constant, the optical phase, ϕ, can be obtained as follows:

$$\phi = \cos^{-1}\left(\frac{I - A}{B}\right). \tag{2}$$

When equation (2) is used for estimating mechanical strain from an EFPI sensor output signal, the arccosine function, however, has a finite range between 0 and π. Accordingly, there exist discontinuous points. Because of this kind of discontinuity, direct evaluation of dynamic strain is not possible. Therefore, information about the direction of structural strain is necessary for solving the discontinuity problem. This directional information can be obtained from any other sensors that can produce a real strain rate. Among the several kinds of sensors, piezoelectric material is chosen for use in this paper. The patch-type EFPI sensor system considered in this study is a simple combination of two existing sensors: an EFPI and PZT. By using the EFPI sensor signal and strain directional information, the optical phase, which corresponds to the mechanical strain, can be obtained as follows:

$$\phi_n = \phi_{n-1} + \mathrm{sgn}(\dot{\varepsilon}) \times \left|\cos^{-1}\left(\frac{I_n - A}{B}\right) - \cos^{-1}\left(\frac{I_{n-1} - A}{B}\right)\right| \tag{3}$$

where ϕ_n ($=2ks_n$) is the optical phase at the nth sampling step. The air cavity length, s, can be calculated using the optical phase, and then the strain can be obtained from the air cavity length. A high pass filtering should be applied to remove any possible error that can arise from the phase accumulation.

For the verification of the proposed phase tracking method, the characteristics of the proposed method are investigated through numerical simulation. The output intensity of an example system is assumed to be $I = A + B\cos(\phi_0 + \phi(t))$. The simulation parameters are defined in table 1.

In order to obtain the exact optical phase, we need exact values for A and B. However, in many practical situations, we may not have exact values for A and B. Therefore, the effects of errors in A and B on the tracking error should be examined. First, the exact case is simulated and the result is shown in figure 2. By using the phase tracking method we can recover the vibration signal accurately even if the output intensity of the example system is highly non-linear. The reconstructed dynamic strain has the same waveform and the errors at strain peaks are within 5% (7.5 $\mu\varepsilon$). The discretization and phase accumulation are main causes of this error. If we can get exact parameters and noise-free data within sufficiently short time intervals, the errors can be further reduced.

Secondly, cases for inexact A and B are simulated. 10% errors in the estimation of A and B are assumed. Figure 3 shows the simulation results for the case in which A is 10%

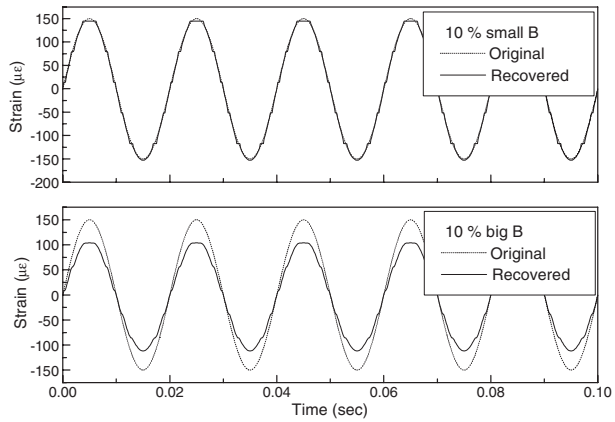

Figure 4. Simulation result with 10% error in B.

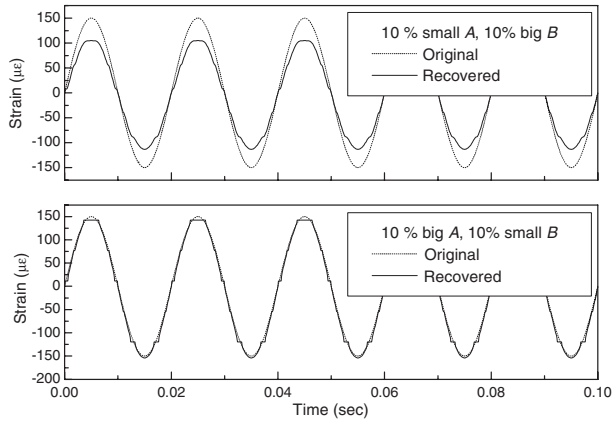

Figure 5. Simulation result when both A and B have 10% errors.

bigger or smaller than the exact value. This means that the median value is incorrect. The peak strain errors are 15.5% (23.3 $\mu\varepsilon$) at a positive peak and 10.3% (15.5 $\mu\varepsilon$) at a negative peak for 10% smaller A, and these become 13.1% (19.7 $\mu\varepsilon$) at a positive peak and 9.7% (14.6 $\mu\varepsilon$) at a negative peak in the case of 10% bigger A. In the case of incorrect B, the peak strain error mainly comes from the calculation of the arccosine. If B is bigger than the exact value, the arccosine value is underestimated and we get overestimated output if B is smaller than the exact value. The peak strain errors for 10% smaller B are 3.4% (5.1 $\mu\varepsilon$) and 1.8% (2.7 $\mu\varepsilon$) at positive and negative peaks, respectively, and they become 30.7% (46.1 $\mu\varepsilon$) at a positive peak and 25.5% (38.3 $\mu\varepsilon$) at a negative peak in the case of 10% bigger B, which are shown in figure 4. In the case where both A and B have errors, the simulation result is similar to that for the incorrect B case. Figure 5 is the simulation result when both A and B have 10% errors.

From the simulation results, it can be inferred that the parameter B in equation (3) is the dominant factor in the error at peak strain, and a slightly small value is favorable for small estimation error. In addition to parameters A and B, the sampling frequency and strain amplitude are other factors in the phase tracking error. The strain amplitude is related to the interferometric non-linear output, and it is dependent on the gage length and the air cavity length—which can be manually

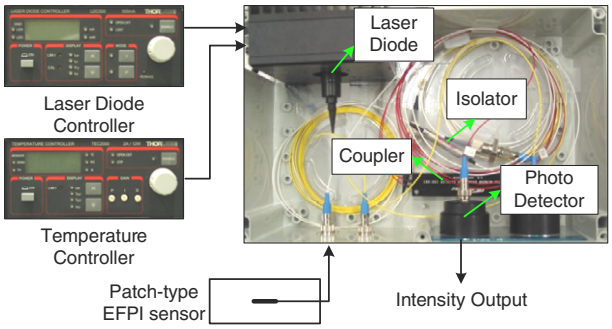

Figure 6. EFPI sensor system.

controlled to a small extent. If we fabricate an EFPI sensor with small gage length, an extremely distorted intensity signal can be prevented. The amplitude of the optical phase for the above example system is about 2.3π. In this case, a vibration signal within 200 Hz can be tracked with 20% peak error, which can be reduced below 5% if the sampling frequency is doubled. In the result, if the parameters A and B are not closely estimated, the proposed phase tracking method cannot guarantee exact dynamic strain values; however it can be used practically for vibration control when the dynamic strain does not exceed 200 Hz frequency and 3π optical phase amplitude.

3. Patch-type EFPI sensor system utilizing PZT

The patch-type EFPI sensor system is proposed for the phase tracking method. An EFPI sensor is attached on PZT, which produces strain rate information. The patch-type EFPI sensor system consists of PZT, an EFPI sensor and an EFPI sensor system, which has a 1310 nm laser diode, an isolator, a photodetector, a 2 by 1 coupler, a laser diode controller and a temperature controller. The overall configuration is shown in figure 6.

The on-line phase tracking experiment has been performed using a composite plate model. The details of the test model will be described in the next section. The base PZT patch has 20 mm width and 50 mm length, and the fabricated EFPI sensor is bonded on the center of the PZT. An electric strain gage and a laser Doppler vibrometer (LDV: QFV303/3001, Polytec) are used for comparison purposes. The location of each sensor is shown in figure 7. The plate is excited with its natural frequency, and the mechanical strain is recovered in real time using the present phase tracking method, using a digital signal processing (DSP) board (DS1103, dSPACE).

To begin with, the PZT output is observed in order to check the hysteretic behavior. The relation of measured PZT output to displacement is shown in figure 8. The hysteretic behavior is observed from these figures. In addition, the PZT output grows to saturation, as the excitation amplitude increases. The hysteretic behavior itself is not worth considering in the phase tracking, because we just need the information of the sign of the strain rate. Hence, the PZT can be used in the phase tracking if the directional information can be extracted from the output. Simply, the differentiation of the PZT signal can be tried, as shown in figure 9. In this case, we have to check whether the differential output corresponds to the strain rate. Ideally,

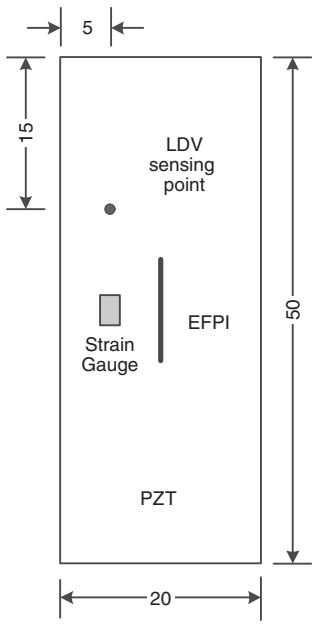

Figure 7. Sensor placement.

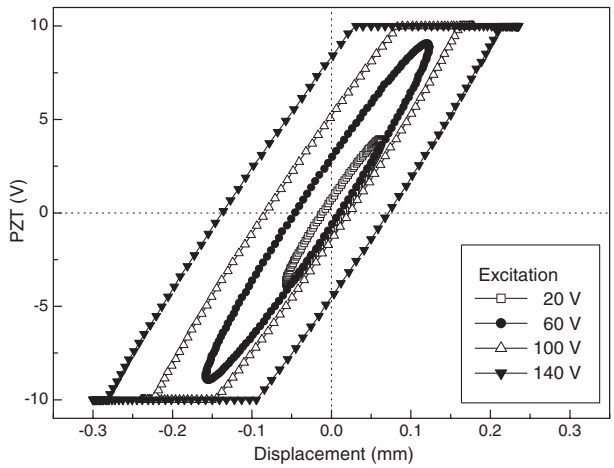

Figure 8. Relation between PZT output and the displacement.

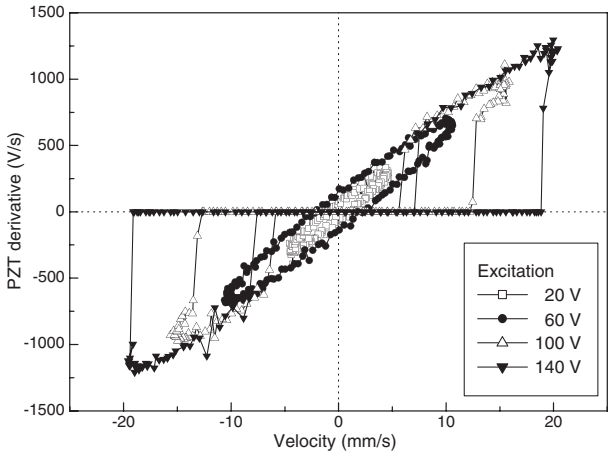

Figure 9. Relation between PZT derivative and velocity.

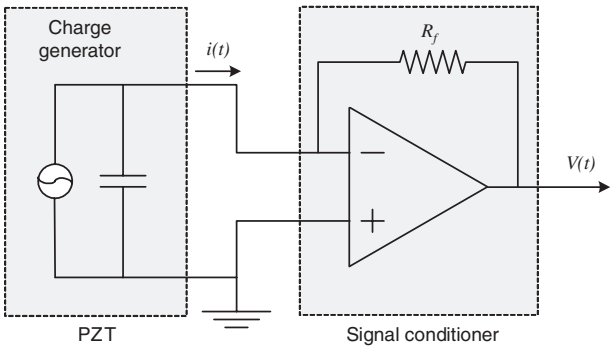

Figure 10. PZT and signal conditioner.

it is expected that all data points are located in the first or third quadrant. And the PZT output must be carefully scaled, because the saturation of the PZT output and consequent error in strain rate can pose a serious problem in phase tracking. If we use an appropriately scaled PZT output without saturation, the hysteretic effects on the strain rate can be considered to be slight and the differential PZT signal can be used as a directional information signal.

Another alternative to differentiation is using a signal conditioning circuit. Within its linear region, the PZT generates an electric charge proportional to the strain and the area of the PZT. Accordingly, the PZT can be considered to be a charge generator. An electric circuit using an operational amplifier with theoretically zero input impedance can be used as a signal conditioner [19]. The signal conditioner incorporated with the PZT is shown in figure 10. The output current of the PZT is simply the time derivative of the charge generated by the PZT. The output voltage of the signal conditioner is the negative of the product of the current and the feedback resistance R_{f} as follows:

$$V(t) = -R_{\mathrm{f}} i(t) = -R_{\mathrm{f}} \frac{\mathrm{d}q(t)}{\mathrm{d}t} \propto -R_{\mathrm{f}} \dot{\varepsilon}(t). \qquad (4)$$

Consequently, the output voltage in equation (4) is proportional to the strain rate. The phase tracking method described in equation (3) uses only the sign of the strain rate. Hence, saturation is out of the question—which can be a problem in the direct differentiation approach. The signal conditioner was also tested in a vibration experiment. Figure 11 is the relation of the circuit output to the velocity signal acquired by the LDV. In this case, almost all data points are located in the first and third quadrants. Therefore, the circuit output signal is regarded as the strain rate signal; accordingly the signal conditioning circuit can be effectively used for the proposed phase tracking method.

At this point, the construction of other types of patch-type EFPI sensor can be considered. The key point of the patch-type EFPI sensor is the combination of the EFPI and another sensor material which can produce directional information. The strain gage, which is one of the most widely used and easily obtainable sensors, can be a candidate for being a part of a patch-type EFPI sensor. However, a strain gage for a patch-type EFPI sensor is not so useful: because the strain

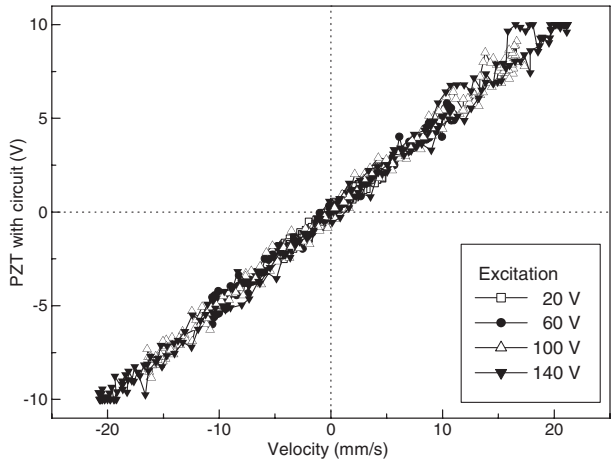

Figure 11. Relation between circuit output and velocity.

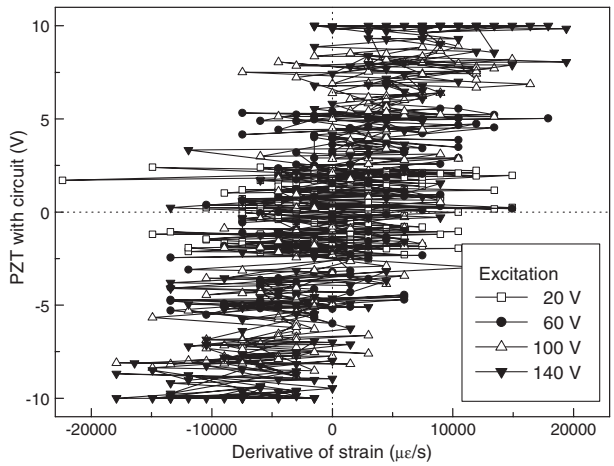

Figure 12. Relation between circuit output and derivative of the strain gage.

gage is not free from electric noise, there can be a serious problem in producing strain rate information. The relation of the circuit output and velocity is almost linear as shown in figure 11; however the relation between the circuit output and the derivative of the strain gage signal is not clear. The derivative of a noisy strain gage signal can produce much more noise as shown in figure 12. Therefore, the construction of a present-type PZT and EFPI sensor is more practical and useful.

Using the proposed phase tracking method and the patch-type EFPI sensor system, an on-line phase tracking test has been performed. Figure 13 shows an example of real time phase tracking. The optical phase can be reconstructed from a highly non-linear EFPI output signal, which cannot be easily obtained in real time using conventional interferometric optical fiber sensors and signal processing techniques. The proposed patch-type EFPI sensor system is free from the hysteresis of the PZT and the interferometric non-linearity. Even if the proposed method cannot cover a broad dynamic range, it can be practically applied to vibration control within a few hundreds of hertz, which is the interesting frequency range in structural vibration control.

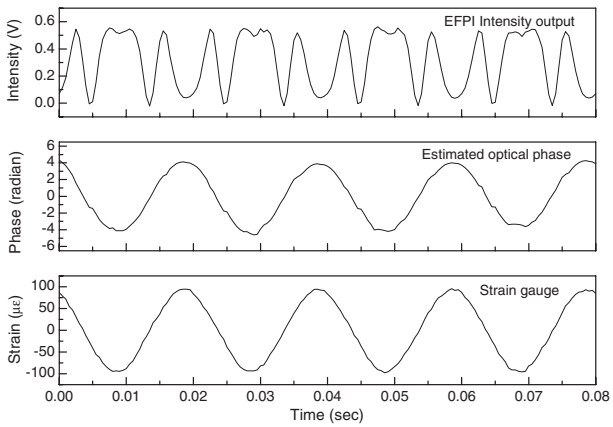

Figure 13. Experimental result of phase tracking.

4. Application of a patch-type EFPI sensor system to flutter suppression

4.1. System description

The test model is a swept-back cantilevered plate with a surface bonded patch-type EFPI sensor and piezoceramic actuators. The base plate is $[90_2/0_2]_s$ graphite/epoxy laminate (CU-125 NS, Hankuk Fiber). Four piezoceramic (C-82, Fuji Ceramics) actuators are bonded on the surface close to the leading edge and one patch-type EFPI sensor ($L = 6$ mm, $s = 14$ μm) is bonded on the surface close to the trailing edge as shown in figure 14.

Wind tunnel testing has been performed in the subsonic wind tunnel at the Department of Aerospace Engineering, KAIST. The wind tunnel is an open-circuit tunnel with effective speed ranges of 9–60 m s^{-1} and it has a closed test section. In order to measure the vibration of the test model, a patch-type EFPI sensor, an electric strain gage and a laser displacement sensor (LB301, KEYENCE) are used. The location of each sensor is described in figure 7. The experimental set-up for the flutter suppression is shown in figure 15. A DSP board (DS1103, dSPACE) is used for the data acquisition and controller implementation. The generated control input is applied to the piezoceramic actuators through a high voltage amplifier (PSZ 700-2, TREK).

4.2. Neural predictive control

The overall structure of the NPC controller is similar to that of [15] as shown in figure 16. The operation of the NPC system comprises two functions: the prediction of the plant output and the minimization of the performance index. First, the prediction of the plant output is performed using the neural network autoregressive external input (NNARX) model [15, 16]. And the next step is the updating of the weights and the calculation of the control input. The generated control input is sent to the plant and the NNARX model. The above procedure is repeated when the controller is turned on.

The NNARX model is used for the plant predictor (or identifier), where the input vector is the same as that of an ARX model. As for its linear counterpart, the predictor is always stable because there is a pure algebraic relationship

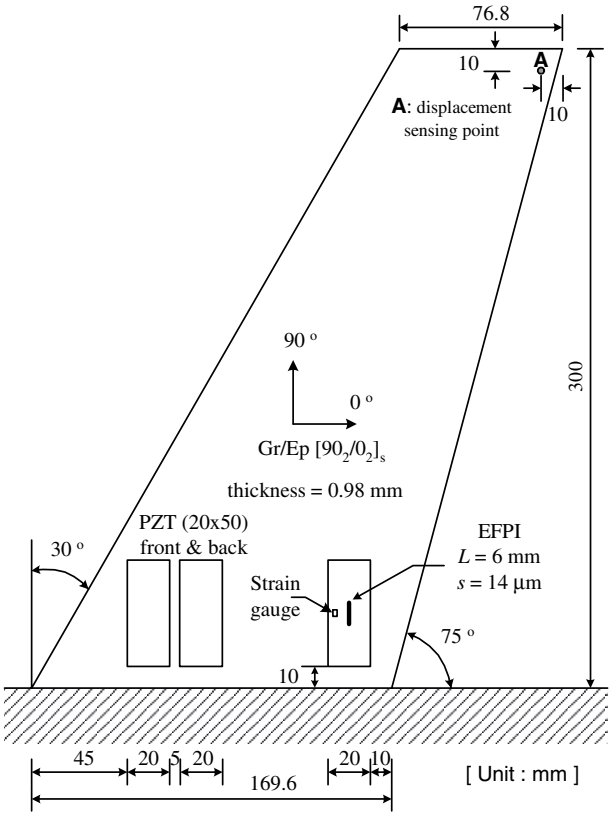

Figure 14. Wind tunnel test model.

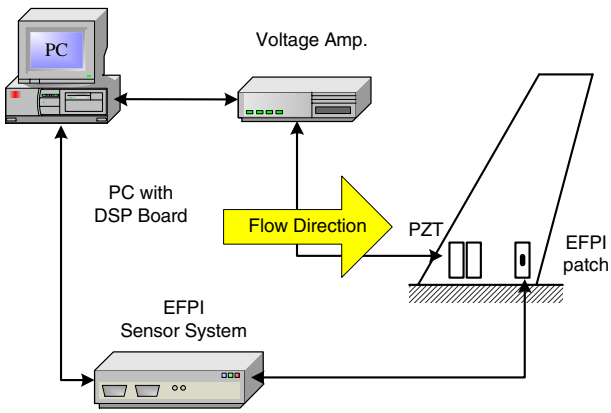

Figure 15. Experimental set-up for flutter suppression.

between prediction and past measurements and inputs. This is particularly important in the non-linear case since the stability issue is much more complex here than for linear systems [14]. The model structure is depicted in figure 17.

The Levenberg–Marquardt back-propagation (LMBP) algorithm is used for learning in order to realize fast real time system identification. This algorithm provides a nice compromise between the speed of Newton's method and the guaranteed convergence of the gradient descent method. The cost function for real time training is the square of the difference between the predicted and actual plant outputs as

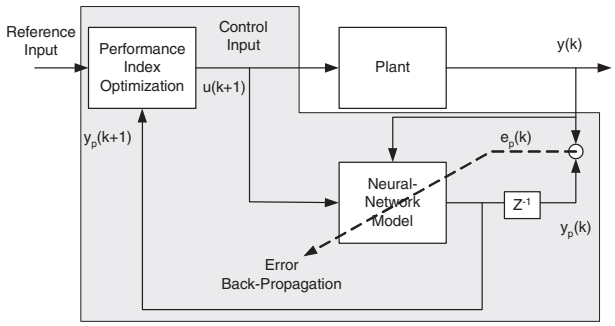

Figure 16. Overall structure of the NPC system.

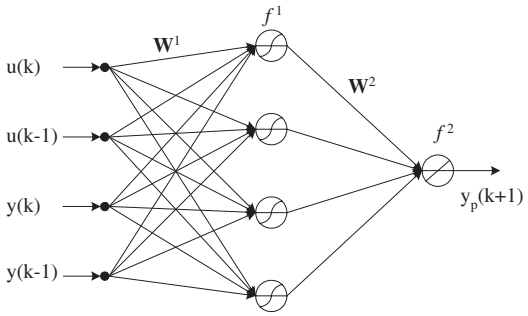

Figure 17. The NNARX model.

follows:

$$F(\boldsymbol{\theta}_k) = e_{\mathrm{p}}^2(k) = (y_p(k) - y(k))^2 \tag{5}$$

where $e_{\mathrm{p}}(k)$ is the prediction error and $\boldsymbol{\theta}_k$ is the vector composed of all weights in the network—that is, all elements of $\mathbf{W}^1$ and $\mathbf{W}^2$. The weights of the network are updated through LMBP as follows:

$$\boldsymbol{\theta}_{k+1} = \boldsymbol{\theta}_k + \Delta\boldsymbol{\theta}_k = \boldsymbol{\theta}_k - [\mathbf{J}^{\mathrm{T}}(\boldsymbol{\theta}_k)\mathbf{J}(\boldsymbol{\theta}_k) + \lambda\mathbf{I}]^{-1}\mathbf{J}^{\mathrm{T}}(\boldsymbol{\theta}_k)e_{\mathrm{p}}(\boldsymbol{\theta}_k) \tag{6}$$

where $\mathbf{J}$ is the Jacobian matrix, $\mathbf{I}$ is the identity matrix and λ is the parameter for determining the search (or update) direction. As λ is increased, the direction will move from the Gauss–Newton direction ($\lambda = 0$) toward the gradient descent direction ($\lambda = \infty$) with zero learning rate [14]. Accordingly, the Levenberg–Marquardt algorithm can be a compromise between the Newton's method and the gradient descent method.

After completing the updating procedure, the one-step-ahead prediction for the plant output is performed. The next step is the generation of the control input. The calculation of the control input is based on the minimization of the performance index—which is generally composed of the square of the predicted output and the square of the change in the control signal as follows:

$$\phi = \sum_{i=N1}^{N2}(y_p(k+i))^2 + \rho\sum_{i=1}^{Nu}(u(k+i-1) - u(k+i-2))^2 \tag{7}$$

where $N1$ is the minimum costing horizon, $N2$ is the maximum costing horizon, Nu is the control horizon, ρ is the control input weighting factor and $u(k)$ is the control input of the present time step [20]. In most cases, $Nu = 1$ is sufficient

Table 2. Modal frequencies of the test model.

Mode No	Modal frequency (Hz)		
	Experiment (plate w/front PZT)	Experiment (plate w/all PZT)	MSC/ NASTRAN
1	11.91	12.16	11.93
2	48.64	49.14	48.46
3	84.31	84.86	83.03
4	120.16	119.77	128.16

to achieve acceptable performance, and $N1 = N2 = 1$ is used for fast real time calculation. The Newton–Raphson method is applied to the minimization of the performance measure:

$$u(k+1) = u(k) - \left(\frac{\partial^2 \phi}{\partial u^2}(k)\right)^{-1} \frac{\partial \phi}{\partial u}(k). \tag{8}$$

After finishing control input calculation, the generated input is fed to the plant and NNARX model to progress toward the next time step.

4.3. Experimental results and discussion

First, modal testing was performed and compared with the result of the MSC/NASTRAN. The material properties of CU-125 NS are as follows:

$$E_1 = 119 \text{ GPa}, \qquad E_2 = 8.67 \text{ GPa},$$
$$G_{12} = G_{13} = 5.18 \text{ GPa}, \qquad G_{23} = 3.29 \text{ GPa},$$
$$\nu_{12} = 0.31, \qquad \rho = 1570 \text{ kg m}^{-3}, \qquad t = 0.1225 \text{ mm}. \tag{9}$$

The structural effects of PZT and optical fiber were assumed to be negligible, so only the base plate is considered in the analysis. Six by twelve QUAD4 2D shell elements are used for normal mode analysis. The experimental and analytic modal frequencies are shown in table 2. The experimental modal frequencies are close to the analytic results.

The MSC/NASTRAN was also used for the aeroelastic analysis. The aeroelastic analysis can be subdivided into two methods. One is frequency domain analysis: the V–g method. The other is time domain analysis: the time integration of the aeroelastic equation. Frequency domain and time domain methods have different approaches, but these methods give similar solutions for linear aeroelastic problems [21]. Because the frequency domain analysis has the advantages of less computation time, simple analysis procedure and ease of physical interpretation, the V–g method is applied and the MSC/NASTRAN [22] is used for linear aeroelastic analysis. The V–g plot is shown in figure 18. It can be seen that the second mode becomes unstable as the airflow speed increases, and the flutter speed is $V_F = 33.5 \text{ m s}^{-1}$. Another particular characteristic for an aeroelastic system is that frequency changes according to airflow speed, which is shown in figure 19, the V–f plot.

When the test model is exposed to the aerodynamic loading in the wind tunnel, air damping is dominant and the aeroelastic system is stable in the case where the airflow speed is below 30 m s^{-1}. As the airflow speed increases, limit cycle oscillation occurs and the vibration amplitude increases

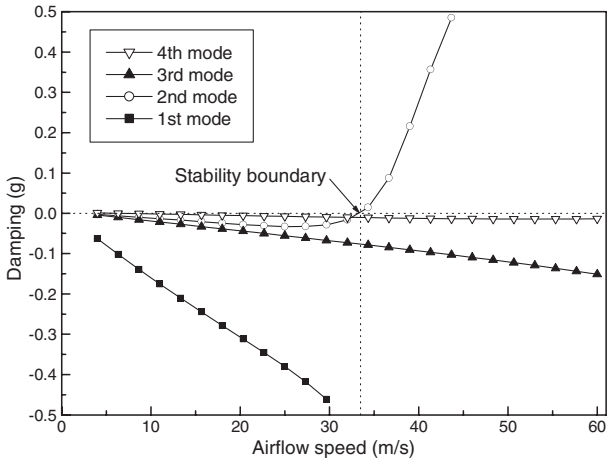

Figure 18. V–g plot of the test model.

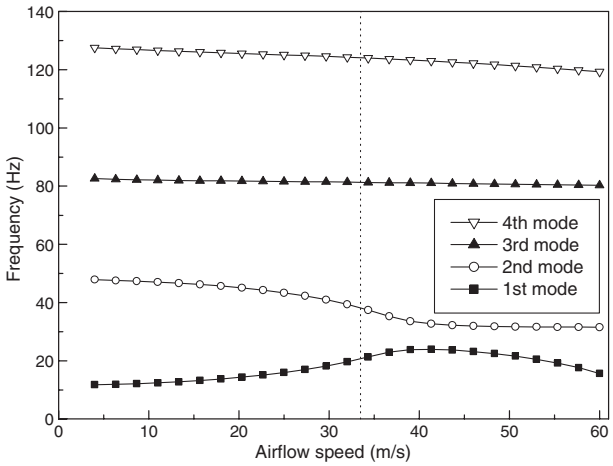

Figure 19. V–f plot of the test model.

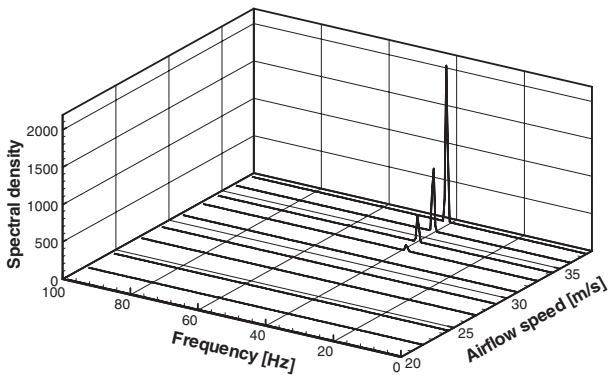

Figure 20. Power spectra of strain versus airflow speed.

according to the airflow speed. Power spectra of the strain against airflow speed are shown in figure 20. It can be found that the vibration energy is concentrated in the flutter mode and increases according to the airflow speed.

A change of the dynamic characteristics appears when the airflow speed is around 33 m s^{-1}. In the case where the

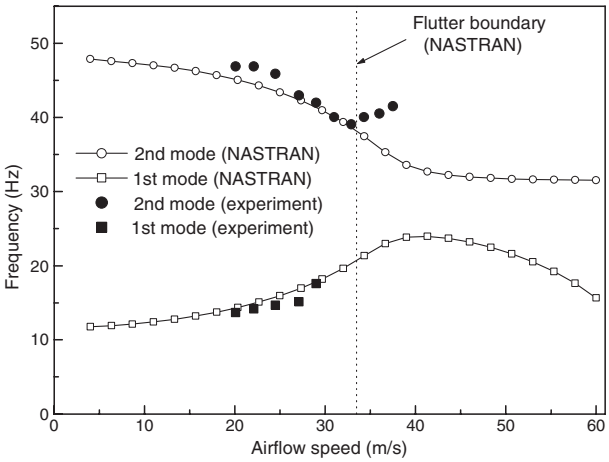

Figure 21. The first and the second modal frequencies of the test model.

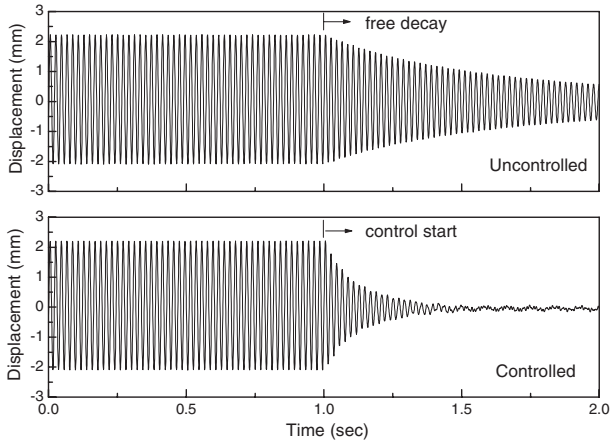

Figure 22. Control result in the still air.

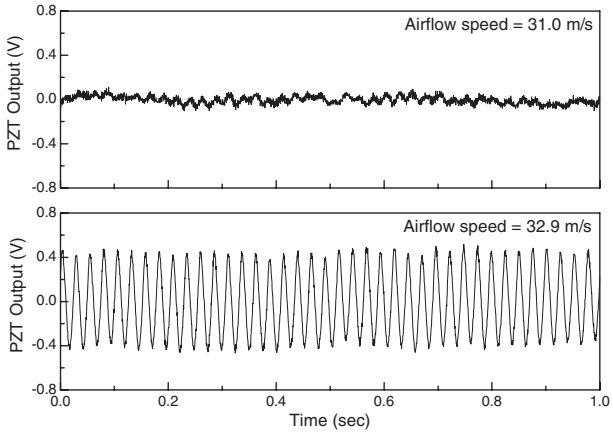

Figure 23. Uncontrolled time history of the PZT signal.

airflow speed is over 33 m s^{-1}, the limit cycle oscillation starts to be observable with the naked eye. Therefore, it can be inferred that the flutter boundary exists around the air speed of 33 m s^{-1}. In general, linear flutter analysis predicts the flutter speed at a lower value than the actual flutter speed. However, the experimentally obtained flutter speed (33 m s^{-1}) is slightly lower than the analysis one (33.5 m s^{-1}). Imperfect modeling is considered to be one of the reasons. Only the base structure is modeled in the analysis; the analysis model does not include surface bonded components, and there can be a slight error in the properties of composite prepreg. Therefore exact material properties and modeling could increase the accuracy of the flutter analysis.

Another phenomenon that we can observe is changes of modal frequencies. The first and the second modal frequencies are compared with analytic results in figure 21. The experimental modal frequencies are close to analytic results when the airflow speed is below the flutter boundary. As the airflow speed increases, the vibration energy is concentrated on the second mode. Therefore, identification of other modes is difficult except for the second mode. And a noticeable phenomenon is that the changing direction of the second modal frequency is opposite to the analytic result. The flutter speed can be calculated via a linear analysis; however post-flutter behavior is a non-linear phenomenon, and accordingly non-linear analysis is necessary for the prediction of the post-flutter behavior. The flutter and post-flutter behavior are well classified and described by Marzocca *et al* [23]. They studied the effects of structural and aerodynamic non-linearities on the character of limit cycle oscillation, and investigated the implication of the incorporation of a control capability for both the flutter boundary and the post-flutter behavior of two-dimensional supersonic lifting surfaces. In the present study, V–g analysis, which is a linear tool, is used. Therefore, the analytic result does not guarantee a reliable result for the post-flutter phenomenon. The point where the second modal frequency takes the opposite changing direction can be another clue to the flutter boundary. The boundary of this discrepancy is 33 m s^{-1}. It is consistent with the airflow speed where large amplitude limit cycle oscillation arises.

Before the flutter suppression experiment, vibration control in the still air was performed. The phase tracking was applied and used as a feedback signal. Figure 22 is the time history of the displacement signal.

The flutter suppression experiment was started from $U_\infty = 31.0$ m s^{-1}, which is just below the flutter speed. The strain gage signal contains a large amount of electric noise; therefore the PZT sensor signal is mainly used for analysis of experimental results. The vibration level does not increase until the airflow speed is increased to 31.0 m s^{-1}. If the airflow speed is increased over 32.9 m s^{-1}, limit cycle oscillation is observed as shown in figure 23. The designed controller is turned on from $U_\infty = 31.0$ m s^{-1}. The controlled time history is shown in figure 24, and the power spectra for uncontrolled and controlled cases at $U_\infty = 32.9$ m s^{-1} are shown in figure 25. By applying the designed control system, the vibration amplitude at $U_\infty = 32.9$ m s^{-1} is reduced to the level of pre-flutter. The peak response in the power spectrum is greatly decreased. In addition, the neural predictive controller showed characteristics of a general purpose controller; the same controller was used in the vibration control in the still air and the flutter suppression. The second modal frequency in the still air is 48.6 Hz and it decreases to 40 Hz at $U_\infty = 33$ m s^{-1}. The designed controller showed good performance in both cases.

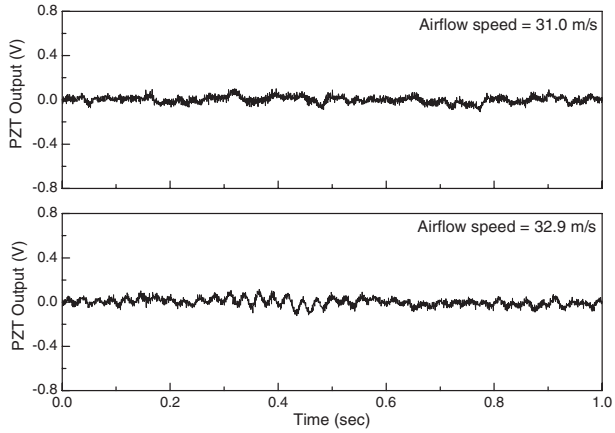

Figure 24. Controlled time history of the PZT signal.

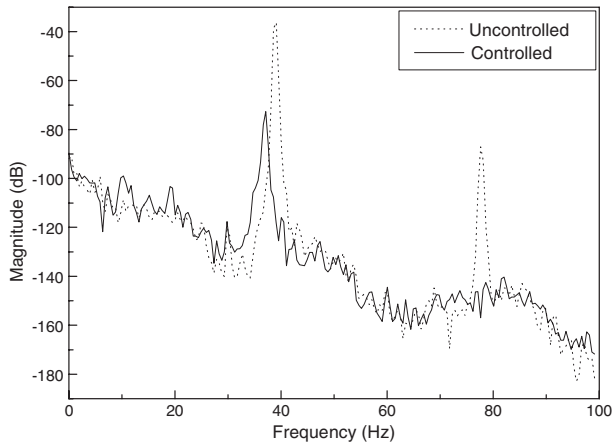

Figure 25. Power spectra of the PZT signal ($U_\infty = 32.9$ m s^{-1}).

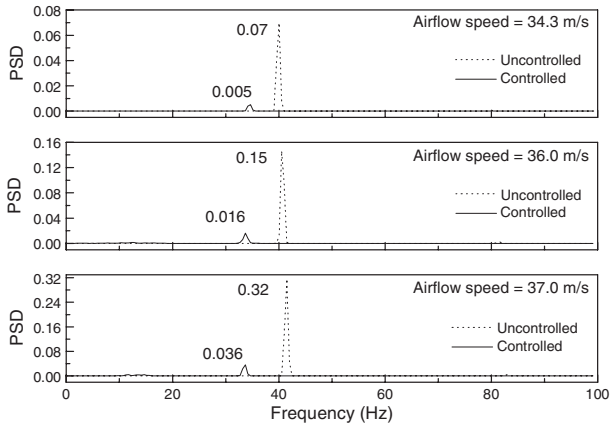

Figure 26. Power spectra of the PZT signal at airflow speeds over the flutter boundary.

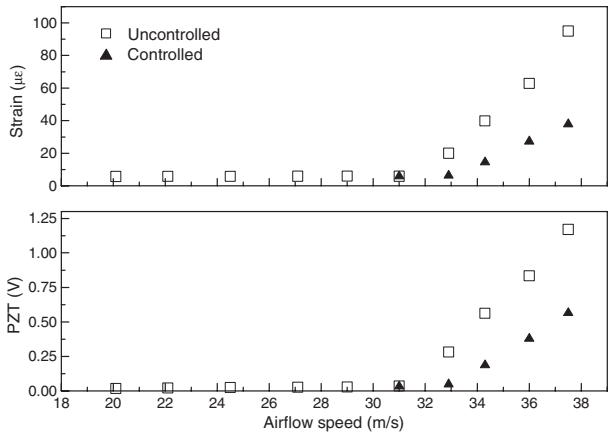

Figure 27. RMS value of strain and PZT signal.

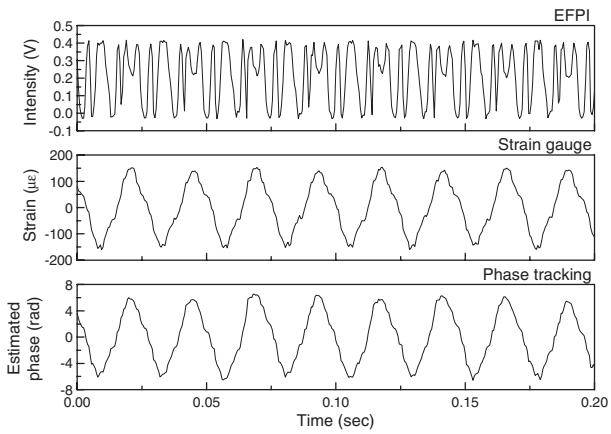

Figure 28. Intensity and estimated optical phase signal.

The control performance can be validated in time and frequency domains as shown in figures 24 and 25. The flutter mode is close to the second structural mode and we can obtain a quantitative result if the peak response is analyzed. Table 3 and figure 26 show the control performance in the post-flutter region.

If the airflow speed is increased over 36.0 m s^{-1}, the ratio of controlled peak response to uncontrolled peak response becomes 0.11 and its square root becomes about one third—which means that the control system reduces the vibration amplitude to one third of that in the uncontrolled case. Another way of investigating the control performance is using RMS (root mean square) values. Figure 27 shows the RMS values of the strain and PZT output over the entire experimental range. From this plot, it can be found that the onset of the flutter is delayed. From time domain data, the flutter boundary is regarded as about $U_\infty = 33$ m s^{-1}. However, the RMS values for the uncontrolled case are beginning to increase at around $U_\infty = 31.0$ m s^{-1}. For the controlled case, the increasing point is considered to be delayed by about 2 m s^{-1}. Hence, we can expect the flutter boundary to be increased by about 6.5% by applying the NPC system and phase tracking method. The performance of the phase tracking is shown in figure 28. The original EFPI sensor signal shows highly non-linear behavior but, on the other hand, the estimated phase signal has the same waveform as the strain gage signal.

5. Conclusion

In the present study, the development of a patch-type EFPI sensor system and its application to flutter suppression have

Table 3. Control performance at airflow speeds over the flutter boundary.

Airflow speed (m s^{-1})	$\frac{\text{Controlled peak response}}{\text{Uncontrolled peak response}}$	$\sqrt{\frac{\text{Controlled peak response}}{\text{Uncontrolled peak response}}}$
32.9	0.015	0.123
34.3	0.074	0.272
36.0	0.111	0.334
37.5	0.114	0.338

been investigated. An on-line phase tracking method was proposed for the purpose of extracting dynamic mechanical strain information from non-linear sensor signals in real time. The proposed method can be practically applied to vibration control within a few hundreds of hertz (frequency). A patch-type EFPI sensor system was constructed and applied to flutter suppression. The proposed patch-type EFPI sensor system is free from the interferometric non-linearity of the EFPI sensor and the hysteresis of PZT. By applying a neural predictive controller, an increase of 6.5% in flutter boundary is obtained. The neural predictive controller showed the special quality of the general purpose controller: it showed good performance in the still air and the same control system successfully suppressed flutter of an aeroelastic system which has a flutter frequency about 10 Hz lower than the second modal frequency. The stability boundary and the reliability of an aeroelastic system could be increased by integrating smart materials into advanced structures.

Acknowledgment

The present study was supported by a grant from the National Research Laboratory Program of the Ministry of Science and Technology, Korea. The authors gratefully acknowledge this support.

References

[1] Murphy K A, Gunther M F, Vengsarkar A M and Claus R O 1991 Quadrature phase-shifted, extrinsic Fabry–Perot optical fiber sensors *Opt. Lett.* **16** 273–5

[2] Tran T A, Greene J A, Murphy K A and Bhatia V 1995 EFPI manufacturing improvements for enhanced performance and reliability *Proc. SPIE* **2247** 312–23

[3] Lo Y L and Sirkis J S 1997 Passive signal processing of in-line fiber Etalon sensors for high strain-rate loading *J. Lightwave Technol.* **15** 1578–86

[4] Kim S H, Lee J J and Kwon D S 2001 Signal processing algorithm for transmission-type Fabry–Perot interferometric optical fiber sensor *Smart Mater. Struct.* **10** 736–42

[5] Kwon I B, Kim C G and Hong C S 1999 A digital signal processing algorithm for structural strain measurement by 3×3 passive demodulated fiber optic interferometric sensor *Smart Mater. Struct.* **8** 433–40

[6] Kim D H, Han J H, Yang S M, Kim D H, Lee I, Kim C G and Hong C S 2003 Optimal vibration control of a plate using optical fiber sensor and PZT actuator *Smart Mater. Struct.* **12** 507–13

[7] Kim D H, Han J H, Kim D H and Lee I 2004 Vibration control of structures with interferometric sensors non-linearity *Smart Mater. Struct.* **13** 92–9

[8] Dowell E H, Crawley E F, Curtiss H C Jr, Peters D A, Scanlan R H and Sisto F 1993 *A Modern Course in Aeroelasticity* (Dordrecht: Kluwer–Academic)

[9] Waszak M R and Srinathkumar S 1995 Flutter suppression for the active flexible wing: a classical approach *J. Aircr.* **32** 61–7

[10] Waszak M R 1998 Modeling the benchmark active control technology wind-tunnel model for active control design application *NASA TP-1998-206270*

[11] Lazarus K B, Crawley E F and Lin C Y 1997 Multivariable active lifting surface control using strain actuation: analytical and experimental results *J. Aircr.* **34** 313–21

[12] Han J H, Tani J and Lee I 2000 Flutter suppression of a lifting surface using piezoelectric actuation *Proc. 2nd Asian–Australasian Conf. on Composite Materials* (Kyongju: KSCM) pp 843–8

[13] Heeg J 1993 Analytical and experimental investigation of flutter suppression by piezoelectric actuation *NASA TP-3241*

[14] Norgaard M, Ravn O, Poulsen N K and Hansen L K 2000 *Neural Networks for Modelling and Control of Dynamic Systems* (Great Britain: Springer)

[15] Jha R and He C 2002 Neural-network based adaptive predictive control for vibration suppression of smart structures *Smart Mater. Struct.* **11** 909–16

[16] Gu D and Hu H 2002 Neural predictive control for a car-like-mobile robot *Robot. Auton. Syst.* **39** 73–86

[17] Tsai P F, Chu J H, Jang S S and Shieh S S 2003 Developing a robust model predictive control architecture through regional knowledge analysis of artificial neural networks *J. Process Control* **13** 423–35

[18] Kim D H, Han J H and Lee I 2004 Application of fiber optic sensor system and piezoelectric actuator to flutter suppression *J. Aircr.* **41** 409–11

[19] Sumali H, Meissner K and Cudney H H 2001 A piezoelectric array for sensing vibration modal coordinates *Sensors Actuators* A **93** 123–31

[20] Haley P and Soloway D 1997 Generalized predictive control for active flutter suppression *IEEE Control Syst.* **17** 64–70

[21] Bae J S, Yang S M and Lee I 2002 Linear and nonlinear aeroelastic analysis of fighter-type wing with control surface *J. Aircr.* **39** 697–708

[22] Rodden W P and Johnson E H 1994 *MSC/NASTRAN Version 68 Aeroelastic Analysis User's Guide* (Los Angeles, CA: MacNeal-Schwendler)

[23] Marzocca P, Librescu L and Silva W A 2002 Flutter, postflutter, and control of a supersonic wing section *J. Guid. Control Dyn.* **25** 962–70